Cell Reports
Physical Science

CellPress
OPEN ACCESS

Article

# Engineering long-term stability into perovskite solar cells via application of a multi-functional TFSI-based ionic liquid

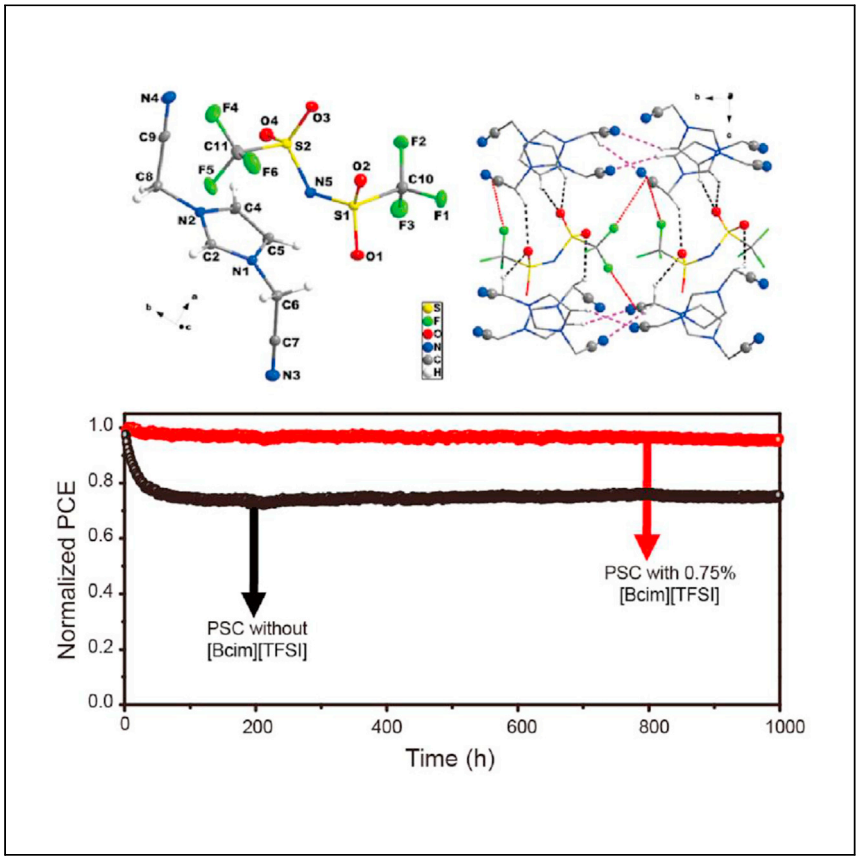


Gao et al. report that the addition of molecular engineered multi-functional ionic liquid into perovskite layer affords high-quality perovskite solar cells with long-term stability and >21% power-conversion efficiency. The unencapsulated devices retain >95% of their original efficiency after 1,000 hours of aging.

Xiao-Xin Gao, Bin Ding, Hiroyuki Kanda, ..., Yaqing Feng, Paul J. Dyson, Mohammad Khaja Nazeeruddin

zhaofu.fei@epfl.ch (Z.F.)
yqfeng@tju.edu.cn (Y.F.)
paul.dyson@epfl.ch (P.J.D.)
mdkhaja.nazeeruddin@epfl.ch (M.K.N.)

## Highlights

A functionalized ionic liquid effectively passivates perovskite films

Low-barrier hydrogen bonds inhibit perovskite deformation

The resulting perovskite solar cells have high efficiency and stability

Engineering long-term efficiency and stability into perovskite solar cells

Gao et al., Cell Reports Physical Science 2, 100475
July 21, 2021 
https://doi.org/10.1016/j.xcrp.2021.100475

Cell Reports
Physical Science

CellPress
OPEN ACCESS

Article

# Engineering long-term stability into perovskite solar cells via application of a multi-functional TFSI-based ionic liquid

Xiao-Xin Gao,[1,2,3,7] Bin Ding,[1,7] Hiroyuki Kanda,[1] Zhaofu Fei,[1,*] Wen Luo,[1,4] Yi Zhang,[1] Naoyuki Shibayama,[5] Andreas Züttel,[1,4] Farzaneh Fadaei Tirani,[1] Rosario Scopelliti,[1] Sachin Kinge,[6] Bao Zhang,[2] Yaqing Feng,[2,3,*] Paul J. Dyson,[1,*] and Mohammad Khaja Nazeeruddin[1,8,*]

## SUMMARY

**Organic-inorganic metal-halide perovskite solar cells (PSCs) have achieved a certified power-conversion efficiency (PCE) of 25.5%. However, long-term stability and air stability of the PSCs are still major concerns and hamper commercialization. Herein, we employ a multi-functional ionic liquid (IL), 1,3-bis(cyanomethyl)imidazolium bis(trifluoromethylsulfonyl)imide ([Bcim][TFSI]), which contains an imidazolium cation functionalized with nitrile (CN) groups and the TFSI anion and is, additionally, able to form an extensive network of low-barrier H bonds, as an additive in perovskite-precursor solutions. Because of a combination of the Lewis-basic CN groups and the hydrophobic TFSI anion in the IL, highly crystalline perovskite films with large grain sizes are obtained. The IL-modified perovskite films afford PSCs with long-term stability and PCEs > 21%. The stability of unencapsulated devices retain >95% of their original efficiency after 1,000 h of aging. This study demonstrates the considerable potential of TFSI-based ILs to improve the performance of PSCs.**

## INTRODUCTION

Perovskite solar cells (PSCs) have attracted considerable attention because of the rapid improvements in their power-conversion efficiency (PCE) from less than 3.8%[1] to greater than 25.5% in the past few years.[2] Despite that rapid development, understanding the origin of the chemical properties of the individual components of PSCs and the interfacial interactions are lacking. Despite extensive research,[3,4] the long-term stability of the PSCs is still a major concern and represents a major bottleneck to commercialization.[5,6]

Perovskite films are traditionally prepared by spin-coating of precursor solutions in polar solvents, such as dimethylformamide (DMF) or dimethyl sulfoxide (DMSO), followed by aging at high temperature. It has been reported that the solvent strongly influences the nucleation kinetics of methylammonium (MA)/formamidinium (FA) lead-iodide salts.[7] Solvent molecules with strong donor groups can coordinate to Pb(II) ions during the formation of the three-dimensional (3D) perovskite structures composed of polymeric $PbI_3^-$ anions and $MA^+/FA^+$ cations, slowing the crystallization process[8] and resulting in the formation of relatively large crystals. To increase the quality of the film, additives have been applied as passivation agents and have been summarized in a recent review.[9] The purpose of passivation is to increase the crystallinity and uniformity of the perovskite film and have fewer defects. As the perovskite film interacts with the electron-transport material (ETM) and hole-transport material (HTM), passivation using multi-functional

[1]Institute of Chemical Sciences and Engineering, École Polytechnique Fédérale de Lausanne (EPFL), 1015 Lausanne, Switzerland

[2]School of Chemical Engineering and Technology, Tianjin University, 135 Yaguan Road, Tianjin 300350, China

[3]Tianjin Collaborative Innovation Center of Chemical Science and Engineering, Tianjin University, Tianjin 300072, China

[4]Swiss Federal Laboratories for Materials Science and Technology (EMPA), 8600 Dübendorf, Switzerland

[5]Department of General Systems Studies, Graduate School of Arts and Sciences, The University of Tokyo, 3-8-1 Komaba, Meguro-ku, Tokyo 153-8902, Japan

[6]Toyota Motor Corporation, Toyota Motor Technical Centre, Advanced Technology Div., Hoge Wei 33, 1930 Zaventum, Belgium

[7]These authors contributed equally

[8]Lead contact

*Correspondence: zhaofu.fei@epfl.ch (Z.F.), yqfeng@tju.edu.cn (Y.F.), paul.dyson@epfl.ch (P.J.D.), mdkhaja.nazeeruddin@epfl.ch (M.K.N.)

https://doi.org/10.1016/j.xcrp.2021.100475

molecules allows a simple additive to not only contribute to the better quality of the film but also improve interfacial interactions, leading to enhanced performance.[10–13] It has been demonstrated that amines with long alkyl chains[11] or fluorous phosphines[12] are particularly effective passivation agents with the Lewis-basic amine or phosphine groups passivating under-coordinated Pb(II) ions. Moreover, the hydrophobic alkyl chains or fluorous groups are hydrophobic and protect the films against moisture. However, passivation using volatile molecules poses both safety and environmental concerns.

Ionic liquids (ILs), being non-volatile salts with high thermal stability, are attractive for a broad range of energy-related applications.[14] ILs have been incorporated into PSCs, including organ-inorganic and all inorganic systems, as passivation agents in the perovskite layer, resulting in improved device stability and performance.[15,16] ILs applied as passivants include those based on alkylammonium,[17–20] aryl-alkylammonium,[21] alkylimidazolium,[22–27] pyridinium,[28] triazolium,[29] and pyrrolidinium cations,[30] with anions including halides, formate, sulfate, hexafluorophosphate ($[PF_6]^-$), and tetrafluoroborate ($[BF_4]^-$).[31] There are several mechanisms by which ILs may improve the quality of perovskite films. During the crystallization process, a small amount of IL additive may influence crystal growth, when the IL forms a eutectic mixture at the latter stage of solvent evaporation during the annealing process of the perovskite films.[23] The inclusion of small molar ratios of ILs does not affect the 3D structure of the perovskite layer, but the quality, especially the uniformity, of the resulting perovskite layer can be significantly improved, resulting in greater efficiencies. In addition to their application as additives in the perovskite layers, ILs have also been applied as effective *p*-dopant additives to improve the electrical properties of the HTM in PSCs[32] or as modification agent for interfacial engineering of electron-transport materials (ETMs).[33,34] Although a number of ILs have already been studied in PSCs, the applied ILs are mostly based on salts with simple alkyl chains in the cation without functional groups attached. So far, the use of the special functionalities of the functional ILs has been limited to a few ILs with fluorous chains, which help to increase the stability of the PSCs because of the hydrophobicity induced by the fluorous chains.[22,25] However, considering the many combinations of functional cations and anions, the application of ILs with functional groups has been elusive. Moreover, $[PF_6]^-$ and $[BF_4]^-$ anions are prone to hydrolysis when exposed to moisture or solvents that contain even traces of water;[35,36] they are also unstable under electrochemical conditions,[37] such as in Li-ion batteries. Consequently, they have been superseded by salts with bis(trifluoromethylsulfonyl)imide ($[TFSI]^-$) anions.[38] ILs with $[BF_4]^-$ anions, such as the commonly used 1-butyl-3-methylimidazolium tetrafluoroborate ([Bmim][$BF_4$]), are hydrophilic, posing difficulties in handling and storage. In addition, they are particularly difficult to purify because water-soluble impurities, such as water NaCl (NaCl is formed during the synthesis by metathesis of [Bmim]Cl with $NaBF_4$) are difficult to remove completely.[39,40] Traces of impurities may significantly affect the reproducibility and quality of experiments that are particularly sensitive to them.[41,42] In contrast to ILs with $[BF_4]^-$ anions, ILs with $[TFSI]^-$ anions are hydrophobic and can be obtained in high yield with high purities. Unlike $[PF_6]^-$ and $[BF_4]^-$ anions, the $[TFSI]^-$ anion is a weak Lewis base, with its O and/or N atoms able to act as both monodentate and bidentate ligands to form dative bonds to alkali/alkali earth metals,[43] transition metals,[44,45] and main group metals (such as Al, Ga, and Sn).[46–48] When ILs with $[TFSI]^-$ anions are used as additives in the perovskite precursor solution, anion coordination to the Pb(II) center should inhibit the formation of the 3D perovskite structures based on repeating $PbI_3^-$/$PbBr_3^-$ units, resulting in the formation of more crystalline perovskite films. The presence of the hydrophobic $CF_3$ groups will also boost the stability against

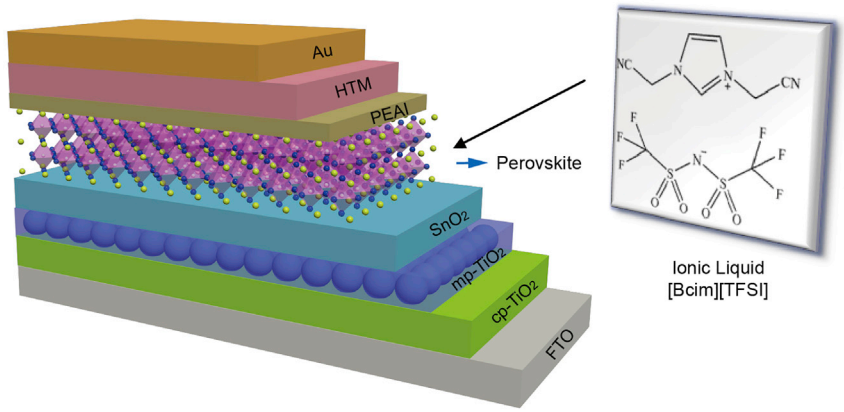


**Figure 1. Device structure with [Bcim][TFSI] as additive**
FTO/cp-$TiO_2$/mp-$TiO_2$/$SnO_2$/perovskite/PEAI/HTM/Au, cp-$TiO_2$, compact $TiO_2$; mp-$TiO_2$, mesoporous $TiO_2$; PEAI, phenethylammonium iodide; HTM, spiro-OMeTAD.

moisture. It is surprising that this kind of hydrophobic ILs have been never explored for PSC applications.

In this work, we prepare the IL 1,3-bis(cyanomethyl)imidazolium bis(trifluoromethylsulfonyl)imide ([Bcim][TFSI]), which contains nitrile (CN) substituents on the cation combined with the hydrophobic $[TFSI]^-$ anion. [Bcim][TFSI] is used as an additive in the triple cation $[(Cs_{0.08}FA_{0.8}MA_{0.12})Pb(I_{0.88}Br_{0.12})_3]$ perovskite-precursor solution (Figure 1). Using an optimized amount of the [Bcim][TFSI], highly crystalline perovskite films with large grain sizes are obtained. The resulting PSC devices show the best PCE of 21.06%, with remarkably improved thermal stability and long-term stability.

## RESULTS AND DISCUSSION

### Morphology of perovskite films

The IL [Bcim][TFSI] is readily obtained by the reaction of trimethylsilyimidazole with chloronitrile, followed by methathesis with Li[TFSI].[49] The [Bcim][TFSI] is insoluble in water, but is highly soluble in polar solvents, such as DMSO or DMF. Addition of the [Bcim][TFSI] into the triple cation $(Cs_{0.08}FA_{0.8}MA_{0.12})Pb(I_{0.88}Br_{0.12})_3$ precursor solution affords a yellow solution. In the initial screening study, PSCs based on triple-cation $(Cs_{0.08}FA_{0.8}MA_{0.12})Pb(I_{0.88}Br_{0.12})_3$ perovskite films with [Bcim][TFSI] ratios of 0.5, 0.75, and 1 mol % were fabricated, with the PSC doped with 0.75 mol % [Bcim][TFSI] showing the best properties.

The morphology and coverage of the perovskite films were investigated by scanning electron microscopy (SEM) (Figures 2A and 2B), and the grain sizes were analyzed with Nano Measurer software (Figure S1; Table S1). The surface of the undoped perovskite film is composed of crystals with an average size of 280 nm (Figure 2A). Interestingly, with the introduction of 0.75 mol % [Bcim][TFSI] in the perovskite-precursor solution, the grain size of the resulting perovskite film increases to 360 nm (Figure 2B). Similar results were observed in perovskite films with 0.5 and 1 mol % ratios of [Bcim][TFSI] (Figure S2). Our result is in agreement with a previous report[26] that shows that addition of a low concentration of [Bmim][$BF_4$] can slightly enlarge the grain size of the perovskite film and improve crystallinity. The cross-sectional SEM analysis of the undoped perovskite film shows the presence of smaller crystals (Figure 2C) compared with IL-doped film, which is also free of pinholes (Figure 2D). The improved crystallinity of the IL-doped perovskite film could be due to the formation of an

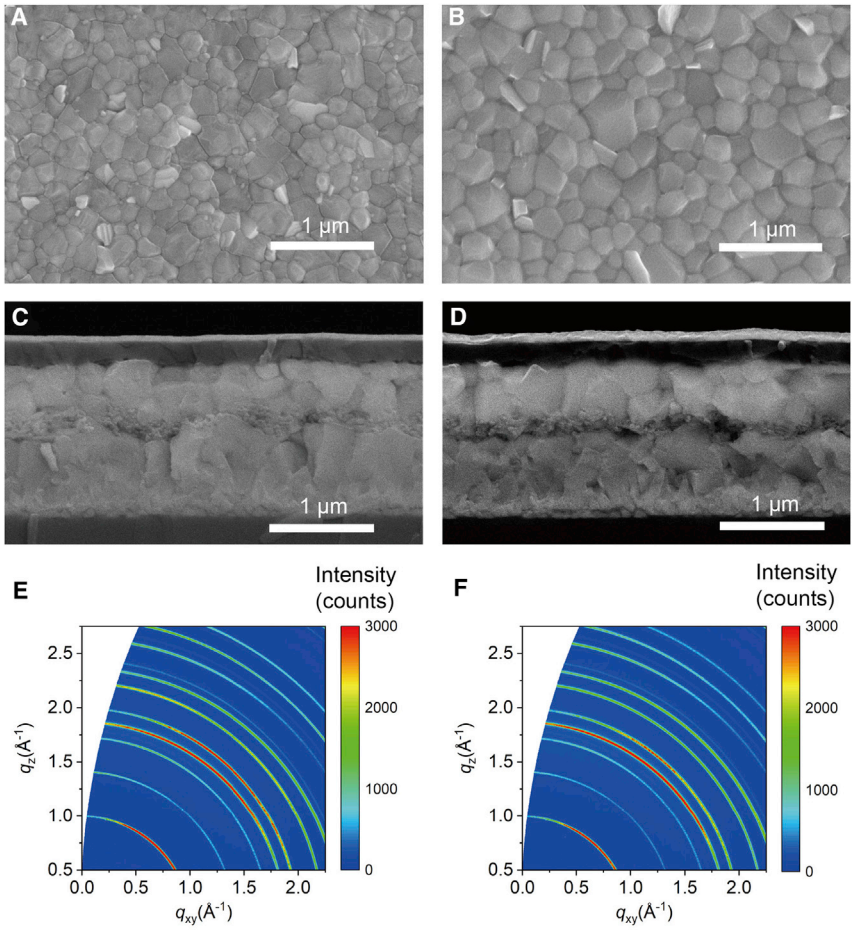


**Figure 2. Morphology of perovskite films**

(A and B) Top-view SEM images of the triple-cation perovskite film without [Bcim][TFSI] (A) and the triple-cation perovskite film with 0.75 mol % [Bcim][TFSI] (B).

(C and D) Cross-sectional SEM images for a PSC fabricated with the triple-cation perovskite film without [Bcim][TFSI] (C) and a PSC device fabricated with the triple-cation perovskite film with 0.75 mol % [Bcim][TFSI] (D).

(E and F) 2D-WAXS patterns of the triple-cation perovskite film without [Bcim][TFSI] (E) and the triple-cation perovskite film with 0.75 mol % [Bcim][TFSI] (F).

eutectic solvent at the end of the aging process because the initial low concentration of [Bcim][TFSI] increases because it is non-volatile, whereas the organic solvent evaporates.[23] The Lewis-basic CN groups on the IL cation and O and N groups on the $[TFSI]^-$ anion may also compete for coordination with the Pb(II) ions during the formation of the 3D perovskite,[8] potentially slowing the crystallization process to afford a higher-quality perovskite film. Furthermore, to determine whether the [Bcim][TFSI] influences the perovskite crystallite orientation, two-dimensional wide-angle X-ray scattering (2D-WAXS) analysis was performed on the perovskite films with and without [Bcim][TFSI]. In both cases, the reciprocal lattice mapping data show almost identical random crystallite orientations, indicating that the [Bcim][TFSI] does not affect the perovskite crystal orientation (Figures 2E and 2F).

## Perovskite films properties

The non-radiative carrier recombination of the perovskite films was analyzed by steady-state photoluminescence (PL) (Figure 3A) and time-resolved PL (TRPL)

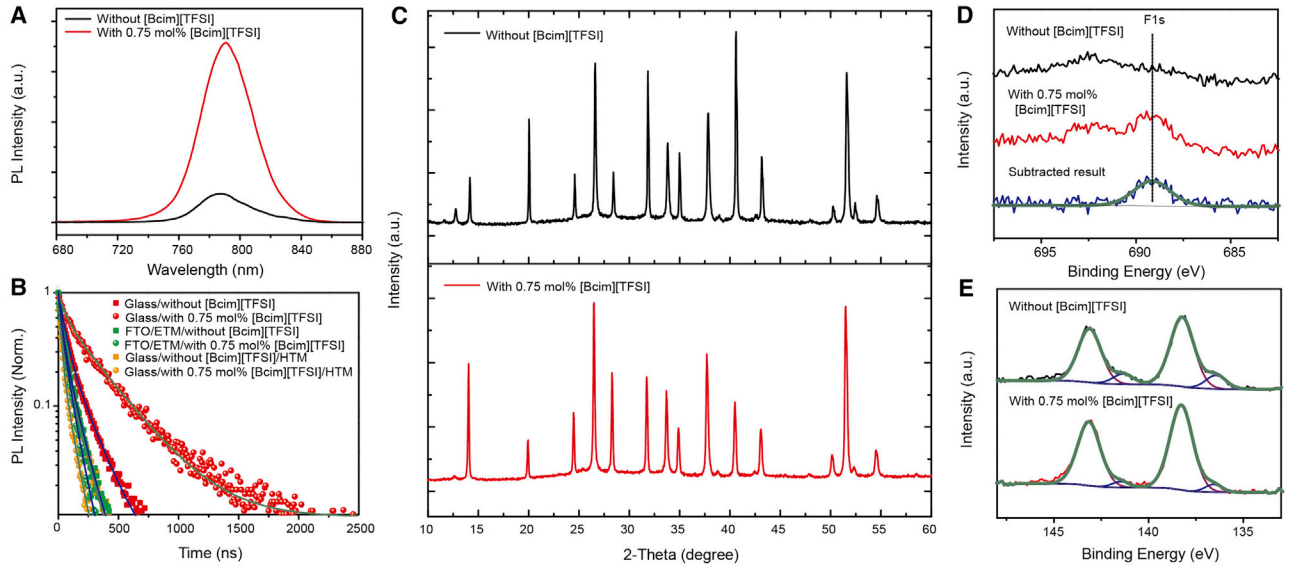


**Figure 3. Perovskite films characterizations**

(A) Steady-state photoluminescence spectra for perovskite films without [Bcim][TFSI] and with 0.75 mol % [Bcim][TFSI].

(B) Time-resolved photoluminescence spectra for perovskite films without [Bcim][TFSI] and with 0.75 mol % [Bcim][TFSI], coated with Glass/perovskite, FTO/ETM/perovskite and Glass/perovskite/HTM.

(C) XRD patterns of perovskite films without [Bcim][TFSI] and with 0.75 mol % [Bcim][TFSI]. XPS of perovskite films on FTO/cp-$TiO_2$/mp-$TiO_2$/$SnO_2$.

(D) F1 s spectra for perovskite films without [Bcim][TFSI] and with 0.75 mol % [Bcim][TFSI].

(E) Pb 4f spectra for films without [Bcim][TFSI] and with 0.75 mol % [Bcim][TFSI] after heating at 150°C in air for 30 min.

(Figure 3B). In addition, the optical properties and film quality were evaluated by ultraviolet-visible (UV-vis) absorption spectroscopy (Figure S3). The PL emission of the undoped film quenched dramatically. In contrast, the intensity of 0.75 mol % [Bcim][TFSI]-doped perovskite film was much stronger (Figure 3A). The peaks in the PL and UV-vis spectra for the IL-doped perovskite film are slightly shifted, probably because of the larger crystal size.

To validate the quality of the perovskite film and the interfacial charge-transfer behavior at the ETM/perovskite/HTM interfaces, biexponential fitting of the TRPL curves were used to quantify the carrier dynamics (Figure 3B; Table S2). The perovskite film doped with 0.75 mol % [Bcim][TFSI] demonstrated a long PL lifetime of 183.8 ns, whereas the PL lifetime for the undoped perovskite film was only 104.1 ns (Table S2). The large increase of PL lifetime indicates that the crystalline quality of the IL-doped film is much improved, with reduced defect states. The PL lifetime of the fluorine-doped tin oxide (FTO)/ETM/IL-doped perovskite film is 52.6 ns, and the PL lifetime of FTO/ETM/IL-free perovskite film is 65.3 ns (Table S2). Similarly, the PL lifetime of glass/IL-doped-perovskite/HTM is short (45.2 ns) compared with that of glass/IL-free-perovskite/HTM (52.7 ns) (Table S2). Therefore, the IL-doped perovskite film between the ETM and HTM exhibits more-efficient PL quenching than the analogous system without IL doping. Hence, doping with [Bcim][TFSI] facilitates the interfacial charge and the hole transfer, which is consistent with reduced defects in the film.

The one-dimensional X-ray diffraction (XRD) patterns of the perovskite films exhibit similar features, which can be indexed to the same crystal system, indicating that the introduction of a low concentration of [Bcim][TFSI] did not change the overall perovskite structure (Figure 3C). However, the 2θ peak at 12.6°, corresponding to

free $PbI_2$, is of much lower relative intensity in the IL-doped perovskite film compared with that of the film without IL doping (Figure S4). In addition, the 2θ peak at 14.1°, corresponding to the 3D perovskite, is a much greater intensity in the IL-doped film than it is in the undoped film. The increase in the intensity of the diffraction peak at (110) plane (Figure 3C) and the decrease in the full width at half-maximum (FWHM) (0.146 versus 0.140) of the perovskite film indicate the improved crystallinity of the perovskite film garnered by introducing 0.75 mol % [Bcim][TFSI]. Moreover, the low-intensity peak at 11.7°, observed only in the undoped film, is assigned to the diffraction of yellow phase (δ-phase) for formamidinium lead triiodide ($FAPbI_3$) in the perovskite film.[50] Overall, the improvement of the crystallinity revealed by the XRD patterns of the IL-doped film is in good agreement with the SEM and PL results.

The presence of [Bcim][TFSI] on the perovskite film was confirmed by X-ray photoelectron spectroscopy (XPS) (Figure 3D). Compared with the undoped perovskite film, the IL-doped film shows a peak at 689.0 eV attributed to F1 s, which is derived from fluorine in the $[TFSI]^-$ anion. Because of the presence of a strong background, the F1 s peak can be better visualized by subtracting the spectrum of the film without [Bcim][TFSI]. In addition, the nitrogen/lead (N/Pb) ratio for the IL-doped perovskite film is about 30% higher than that without the IL (Table S3). The increased N/Pb ratio can be attributed to the introduction of N in both the cation and anion in [Bcim][TFSI], demonstrating the presence of the [Bcim][TFSI] in the perovskite film. This is consistent with the UV-vis/PL shifts, which may be attributed to the presence of [Bcim][TFSI] at the surface of the perovskite film. The presence of [Bcim][TFSI] on the surface of the perovskite film was further confirmed by fluorine nuclear magnetic resonance ($^{19}F$ NMR) spectroscopy. Washing the prepared film (before the treatment with phenethylammonium iodide [PEAI]) with deuterated DMSO ($d_6$-DMSO) and analyzing the obtained solution by $^{19}F$ NMR spectroscopy revealed a singlet at −78.6 ppm corresponding to the $CF_3$ groups on the $[TFSI]^-$ anion (Figure S5), whereas the $^1H$ NMR spectrum of the solution was of a routine nature.[51]

To verify the degradation products of the perovskite film at an elevated temperature, the thermal stability of films without and with IL-doping were investigated by placing the films on a hotplate at 150°C for 30 min in air and then making XPS measurements. As shown in Figure 3E, the initially observed main peaks before heating at 138.5 and 143.4 eV can be ascribed to the Pb $4f_{7/2}$ and Pb $4f_{5/2}$ of Pb–X (X: I, Br, and Cl) bonds in the perovskite films, respectively.[52] After deconvolution, two additional peaks at lower binding energies (136.6 and 141.5 eV) can be observed, which are contributed by metallic Pb.[53,54] Because metallic Pb was not detected in the freshly prepared samples, these metallic Pb species are presumably generated during the degradation process (Figure S6). The presence of metallic Pb is indicative of deficiencies in the iodide in the perovskite lattice. In addition, the metallic Pb species in the film may act as recombination centers.[55,56] Notably, the ratio of metallic Pb in the undoped perovskite film is more than two times greater than that in the IL-doped film (Table S4), indicating that [Bcim][TFSI] significantly improves the thermal stability. With two CN groups attached to the imidazolium cation, [Bcim][TFSI] can be considered an ionic acetonitrile-like compound that can coordinate to the under-coordinated Pb(II) centers to increase the thermal stability of the film. Within the structure of [Bcim][TFSI], the electron-withdrawing CN groups will increase the acidity of the protons in the ring protons and the protons in the $CH_2$ units linking the imidazolium cation and the CN groups, resulting in additional H bonding, further strengthening the interface between the perovskite film and the PEAI/HTM layers (see X-ray crystallography discussion below). In addition, the presence of a highly hydrophobic species with $[TFSI]^-$ anion will reduce unwanted hydrolysis reactions from taking place.

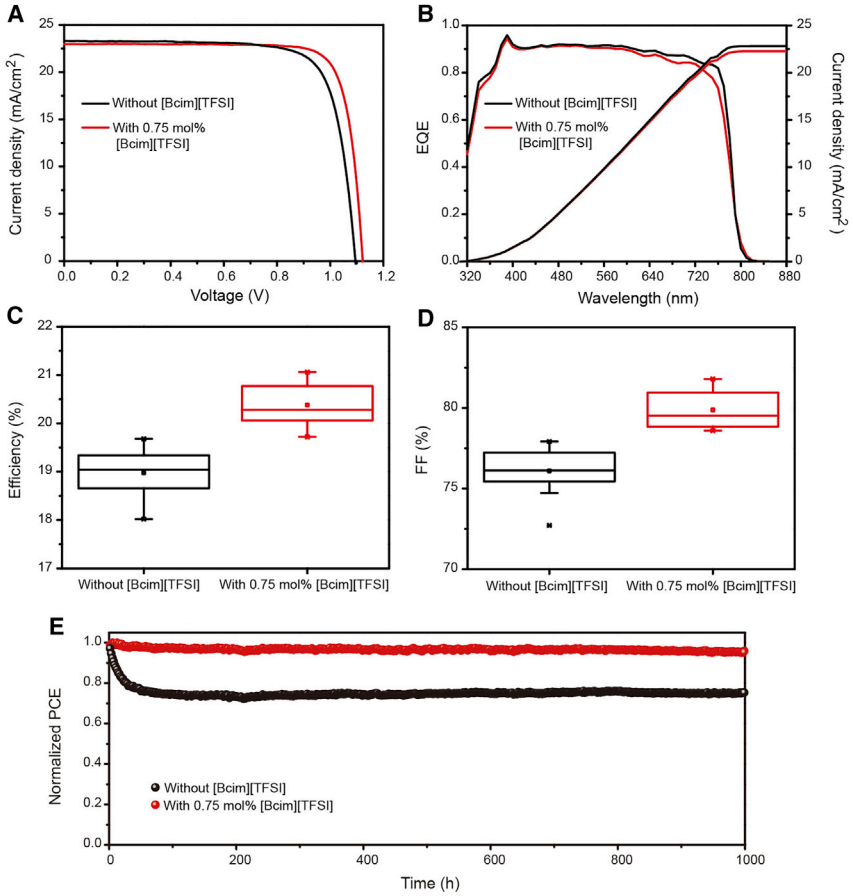


**Figure 4. Photovoltaic performance and stability of devices**

(A) J-V curves of best-performing devices at reverse scans. The scanning speed is 0.1 V $s^{-1}$ and the active area is 0.16 $cm^2$.

(B) EQE spectra of the best-performance devices and the integrated $J_{sc}$ curves of the best-performance devices.

(C and D) Boxplots of PCEs (C) and FFs (D) based on 15 devices each.

(E) Stability study shown as *in situ* measured PCE of the unencapsulated PSCs without and with 0.75 mol % [Bcim][TFSI] for 1,000 h under $N_2$.

## Photovoltaic performance and stability of devices

All PSCs devices were fabricated by treating the films with PEAI, followed by a routine finishing process.[57] From a comparison of the performances of the devices with [Bcim][TFSI] (at three different concentration, i.e., 0.5, 0.75, and 1 mol %), it was found that the optimized [Bcim][TFSI] concentration is 0.75 mol % (Figure S7; Table S5). To investigate the influence of the CN group in the cation, a benchmark IL, 1-ethyl-3-methylimidazolium bis(trifluoromethylsulfonyl)imide ([Emim][TFSI]), was applied at the same concentration (0.75 mol %) as a dopant for the triple-cation PSCs, using the same conditions otherwise. The initial tests show that doping with [Emim][TFSI] resulted in poor performance compared with the results of that doped with [Bcim][TFSI] (Figure S8; Table S6). The photovoltaic performance of the PSCs with 0.75 mol % [Bcim][TFSI] was measured under standard AM 1.5-G solar illumination and compared with devices without IL doping. The current-density-voltage (J-V) curves and corresponding photovoltaic parameters for the champion devices without and with 0.75 mol % [Bcim][TFSI] were recorded (Figure 4A; Table 1). The open-circuit voltage ($V_{oc}$) of the IL-doped PSC exhibits a higher value of 1.12 V

**Table 1. Champion device performance for PSCs without [Bcim][TFSI] and with 0.75 mol % [Bcim][TFSI]**

| Perovskite | VOC (V) | Jsc (mA $cm^{-2}$) | FF (%) | PCE (%) |
|---|---|---|---|---|
| Without [Bcim][TFSI] | 1.09 | 23.30 | 77.22 | 19.68 |
| With 0.75 mol % [Bcim][TFSI] | 1.12 | 22.97 | 81.80 | 21.06 |

compared with that without IL (1.09 V). The short-circuit current density ($J_{sc}$) of the PSC with 0.75 mol % [Bcim][TFSI] is slightly lower than that without IL (22.97 versus 23.30 mA $cm^{-2}$) (Table 1). The fill factor (FF) for the PSC with 0.75 mol % [Bcim][TFSI] is 81.80%, significantly higher than the value of 77.22% for PSC without IL-doping (Table 1). Notably, the FF value of the IL-doped champion device was also higher than PSCs doped with other [$BF_4$]-based ILs recently reported,[26,30] close to the record values experimentally obtained.[11,58] Importantly, the champion IL-doped device affords the best overall performance, with a PCE of 21.06% compared with 19.68% for the PSC without IL doping (Table 1). This enhancement can be ascribed to the reduced photo-generated charge recombination at the perovskite interface, as evidenced by the PL measurements. In general, the hysteresis between forward and reverse scanning is key to the integrated performance of the PSCs. The hysteresis of the PCE is 5% for the PSC without IL doping and 3% for the IL-doped PSC. Apparently, the introduction of [Bcim][TFSI] not only improves the efficiency but also alleviates the hysteresis (Figure S9). Figure 4B shows the spectral dependence of the external quantum efficiencies (EQEs) and the corresponding integrated currents of the PSCs under various conditions. The devices without and with 0.75 mol % [Bcim][TFSI] have similar spectral features and show high EQE values (≈90%) because of the application of same device structure. The trend of the integrated current density for the different devices is consistent with those obtained from the experimental J-V measurements. As a result, an average PCE (20.4%) was achieved from the devices with 0.75 mol % [Bcim][TFSI], which is markedly higher than that without IL doping (19.0%) (Figure 4C). Usually, the FF of PSCs is sensitive to the quality of the perovskite layer, the ETM, and the HTM.[59] A statistical analysis of the FF confirmed that most devices with 0.75 mol % [Bcim][TFSI] demonstrate better overall performance than PSCs do without IL doping (Figure S10). Moreover, the statistical FF of devices with 0.75 mol % [Bcim][TFSI] showed a narrow distribution (Figure 4D). Considering the same ETM and HTM were used for all the devices, the improved average performance of the PSCs is due to the improved quality of the perovskite film. To characterize the density of the defect states, space charge limited current (SCLC) analysis was performed. The trap densities ($n_t$) were calculated using the equation below:[60,61]

$$V_{TFL} = \frac{e n_t L^2}{2\varepsilon_0 \varepsilon} \qquad \text{(Equation 1)}$$

where $L$ is the thickness of the perovskite film, $\varepsilon$ is the relative dielectric constant of perovskite layer, $\varepsilon_0$ is the vacuum permittivity, and $e$ is the elementary charge. The $n_t$ values of the film doped with 0.75 mol % [Bcim][TFSI] and the undoped film were $7.0 \times 10^{15}$ $cm^{-3}$ and $7.6 \times 10^{15}$ $cm^{-3}$, respectively (Figure S11). This indicates that the trap density in the perovskite film was reduced by implementing the IL doping, consistent with the TRPL results.

To investigate the stability of the devices, the steady-state photocurrent density of the PSCs was measured at a fixed bias potential, in which the maximum power output (MPO) was detected in the J-V curve. The photocurrent output of the devices without and with 0.75 mol % [Bcim][TFSI] showed similar performance. Only a

minimal decrease was observed for the device without IL after 125 s, compared with that of the IL-doped device (Figure S12). However, significant differences were observed over extended times. Both PSC devices without and with IL were maintained in a nitrogen atmosphere under a constant illumination of 100 mW $cm^{-2}$. The J-V curves were recorded every 2 h. The device doped with 0.75 mol % [Bcim][TFSI] was much more stable than that without IL doping (Figure 4E). After 1,000 h of continuous light soaking, the MPO values of the IL-doped device maintained >95% PCE compared with 75% for the device without IL doping. The stability of the IL-doped PSC was further compared with that of the IL-free device by storing the devices in the dark at room temperature with a relative room humidity (RH) of 20%–30%. The devices were periodically evaluated to obtain the PCE values. The IL-doped PSC exhibited better overall air stability than the PSC without IL doping (Figure S13). The increased stability of the IL-doped device was also reflected by smaller decreases in PCE and FF values compared with that of the IL-free device (Figure S13).

### Crystal structure of the [Bcim][TFSI]

[Bcim][TFSI] is responsible not only for the increased quality of the perovskite film but also for the improved long-term performance of the PSCs. To determine the origin of the role of the [Bcim][TFSI], the molecular structure of the [Bcim][TFSI] was determined by single-crystal XRD on crystals obtained by an *in situ* crystallization technique.[62] The molecular unit of the [Bcim][TFSI] structure consists of the imidazolium cation with the two $-CH_2CN$ arms in a *trans* orientation along the planar imidazolium ring (Figure 5A). The two $CF_3$ groups in the anion are also *trans* oriented, despite the high symmetry of the cation (Figure 5A).[63] The bond angles and distances in the cation and anion are within the expected range (Tables S7–S10).[49,62,63] Examination of the packing reveals an extensive hydrogen bond network with many $C\equiv N\cdots F$, $C–H\cdots O$ and $C–H\cdots N$ distances in the range of 2.4–3.2 Å (Figures 5B, S14, and S15; Table S11), leading to a highly condensed and stable structure (Figures 5C and S14). It is notable that, within the diverse arrays of hydrogen bonds, many have distances below 2.55 Å, which can be classified as low-barrier hydrogen bonds (LBHBs).[64] By using [Bcim][TFSI] as an additive for the triple-cation perovskite, it is conceivable that these LBHBs will arise at the surface of the perovskite film and at the interface of the perovskite with the ETM, PEAI, and HTM layers, forcing interactions between the H atoms in the $FA^+$ and $MA^+$ cations with the IL. Additional strong hydrogen bonds from the H atoms in the imidazolium cation to the halides in the $PbI_3^-$ and $PbBr_3^-$ fragments might also exist. Overall, these LBHBs could facilitate hydrogen sharing (hydrogen atoms are rigidly locked),[65] increase the rigidity of the entire 3D perovskite, help to prevent lattice distortions, and inhibit phase transformations, consequently contributing to the high stability of the perovskite, as suggested from theoretical studies.[66,67] In addition, the Lewis-basic groups present in the IL may interact with coordinatively unsaturated Pb(II) ions, passivating the perovskite layer, similar to that observed elsewhere.[12,68]

Because the 3D perovskite layer was further treated with a PEAI layer, the [Bcim][TFSI] could also strengthen the interfacial interactions via hydrogen bonding, further contributing to the long-term stability. In addition to hydrogen bonding, the bulky and hydrophobic TFSI anion with two $CF_3$ groups will also increase the hydrophobicity of the perovskite surface, acting as a barrier to repel water. Consequently, the surface is protected from the degradation by the hydrolysis when exposed to moisture.

In conclusion, we incorporated an imidazolium-based IL with CN groups and the $[TFSI]^-$ anion (employed in Li-ion batteries) as an additive in a triple-cation PSCs.

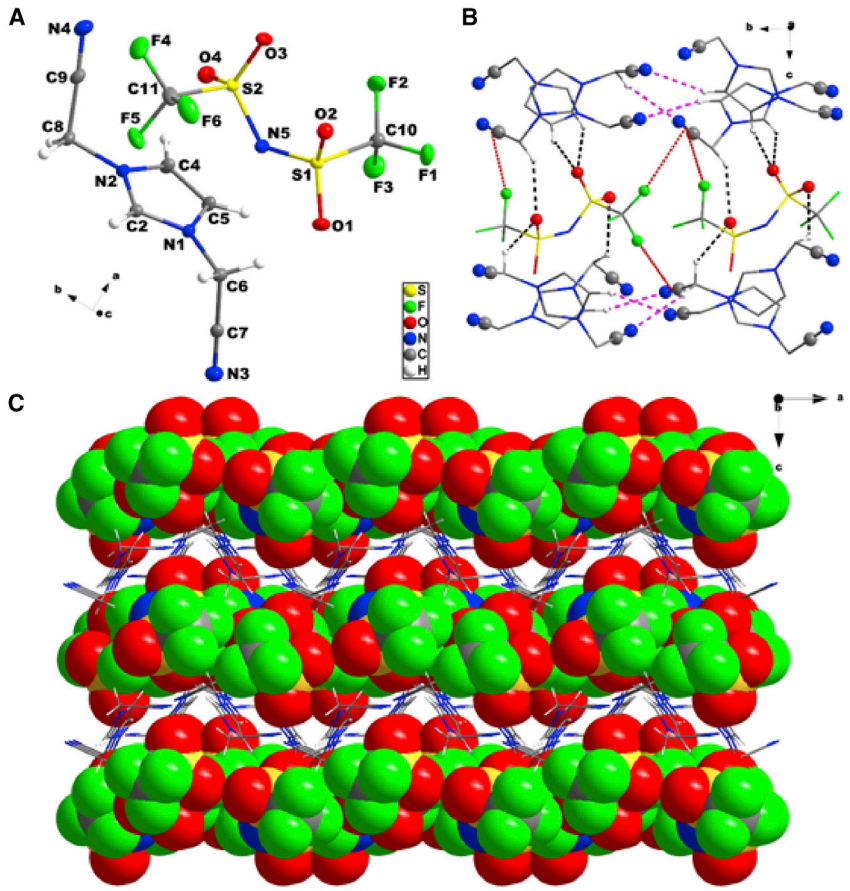


**Figure 5. Crystal structure of the [Bcim][TFSI]**

(A) The asymmetric unit (at the 30% probability level).

(B) The hydrogen-bonding network of the [Bcim][TFSI] in the bc plane.

(C) The $[TFSI]^-$ anion layers clamp the imidazolium cation layers to form a metal-free perovskite-like structure.

A PCE of 21.06% after doping with 0.75 mol % of the [Bcim][TFSI] was achieved with an increased FF and improved long-term stability. The improvement in performance is believed to be due to the presence of the Lewis-basic functional groups in the [Bcim][TFSI], which can potentially coordinate to Pb(II)-ion-retarding crystallization, leading to the formation of larger crystals, passivating the perovskite film. In addition, the $[TFSI]^-$ anion provides an extensive range of strong hydrogen-bonding interactions, further increasing the overall stability of the PSCs, and the hydrophobic nature of the IL can form a protective sheath that further contributes to its long-term stability. To our knowledge, the use of ILs with the highly stable $[TFSI]^-$ anion, rather than the unstable $[PF_6]^-$ and $[BF_4]^-$ anions, is new and offers considerable potential for molecular engineering of perovskite films for PSCs and other applications in the future.

## EXPERIMENTAL PROCEDURES

### Resource availability

#### *Lead contact*

Further information and requests for resources should be directed to, and will be fulfilled by, the lead contact, Mohammad Khaja Nazeeruddin (mdkhaja.nazeeruddin@epfl.ch).

*Materials availability*

Unless otherwise noted, all solvents and reagents were obtained from commercial sources and were used without further purification.

*Data and code availability*

All data supporting the findings of this study are presented within the article and Supplemental information. Crystallographic data of [Bcim][TFSI] have been deposited with the Cambridge Crystallographic Data Centre and correspond to code 2070505. These data can be obtained free of charge via https://www.ccdc.cam.ac.uk/data_request/cif, or by emailing data_request@ccdc.cam.ac.uk, or by contacting the Cambridge Crystallographic Data Centre, 12 Union Road, Cambridge CB2 1EZ, UK; fax: +44 1223 336033). All other data are available from the lead contact upon reasonable request.

## Fabrication of perovskite solar cells

The IL [Bcim][TFSI] used in this study was prepared according to a method in the literature.[49] All other starting materials are commercially available and were used directly without further purification. FTO-coated glass substrates (Nippon sheet glass, TEC8) was cleaned with detergent, deionized water, acetone, and isopropanol in the ultrasonic bath for 10 min. The FTO substrates were treated with an UV/ozone cleaner for 15 min before being used. $TiO_2$ compact layers (cp-$TiO_2$) were deposited onto the clean FTO substrates by spray pyrolysis using a titanium diisopropoxide bis-(acetylacetonate) solution (75% in 2-propanol, Sigma-Aldrich), which was diluted in 2-propanol (99.8%, Acros Organics) at 1:15 volume ratio on 450°C and followed by *in situ* annealing for 30 min. The mesoporous $TiO_2$ (mp-$TiO_2$) solution, was composed of 1 g $TiO_2$ paste (30NR-D, Greatcell Solar) diluted in 10 mL of anhydrous ethanol solution; then, the meso-$TiO_2$ layer was deposited onto the FTO/cp-$TiO_2$ substrate by a one-step spin-coating process at 4,500 rpm for 20 s. After annealing at 125°C for 30 min, the mp-$TiO_2$ films were gradually heated to 500°C in air, and then, they were baked at the same temperature for 20 min to remove organic components. $SnO_2$ layers were prepared by spin coating 0.1 M $SnCl_4$ aqueous (99%, Acros Organics) solution by a one-step process at 3,000 rpm for 20 s; then, the substrates were transferred onto a hotplate and heated between 150°C and 190°C for 1 h. Finally, the FTO/cp-$TiO_2$/mp-$TiO_2$/$SnO_2$ substrates were treated with UV/ozone for 30 min.

The precursor solution (without [Bcim][TFSI]) was prepared by mixing stock solutions of $PbI_2$ (1.190 M, TCI), $PbBr_2$ (0.155 M, TCI), CsI (0.105 M, TCI), FAI (1.040 M, Dyesol), and methylammonium bromide (MABr; 0.155 M, Dyesol) in a mixed solvent of DMF:DMSO = 4:1 (volume ratio). The precursor solutions containing [Bcim][TFSI] were prepared by mixing stock solutions of $PbI_2$ (1.190 M, TCI), $PbBr_2$ (0.155 M, TCI), CsI (0.105 M, TCI), FAI (1.040 M, Dyesol), and MABr (0.155 M, Dyesol) with increasing amount of [Bcim][TFSI] (0.5, 0.75, and 1 mol %) in DMF/DMSO (4:1, volume ratio). For the control experiment applying [Emim][TFSI], the same amount (0.75 mol %) of [Emim][TFSI](Sigma-Aldrich) was used, instead of the [Bcim][TFSI]. Next, the perovskite-precursor solutions were spin coated on the top of the FTO/cp-$TiO_2$/mp-$TiO_2$/$SnO_2$ substrate at 1,000 rpm for 10 s and continuously spun at 5,000 rpm for 30 s, and 100 μL of chlorobenzene was dropped onto the films 15 s before the end of the process. Then, the films were annealed on the hotplate at 100°C for 1 h. After cooling to room temperature, a solution of PEAI diluted in isopropanol (14.9 mg/mL) was spun on the substrate at 4,000 rpm for 30 s. Next, 40 μL of spiro-OMeTAD solution was deposited by spin coating at 4,000 rpm for 20 s on the perovskite film as

the hole-transport layer. The HTM solution was prepared by mixing a stock solution of spiro-OMeTAD in chlorobenzene with solutions of 4-tert-butylpyridine, Li[TFSI], and Co[t-BuPyPz]$_3$[TFSI]$_3$ (FK209, Dyesol) in acetonitrile with a molar ratio of spiro-OMeTAD:FK209:Li[TFSI]:tributyl phosphate (TBP) at 1:0.03:0.5:3.3. Finally, a 70-nm-thick layer of gold was thermally evaporated to form a counter electrode to complete the device fabrication. All the steps used to deposit the perovskite-precursor solution and HTM solution were performed inside a glove box filled with nitrogen to minimize the influence of moisture.

### Film characterization

The morphology and particle size of the films were examined by SEM (FEI Sirion-200) operating at 10 kV. One-dimensional XRD analysis was performed with a D8 Advance diffractometer (Bruker) with Cu Kα radiation (λKα = 1.5418 Å) by measuring the diffraction angle (2θ) between 10° and 60°. 2D-WAXS patterns represented in the reciprocal lattice space were conducted at BL46XU beamline at SPring-8. The sample was irradiated with an X-ray energy of 12.39 keV (λ = 1 Å) at a fixed-incident angle on the order of 2.0° through a Huber diffractometer. The 2D-WAXS patterns were recorded with a two-dimensional image detector (Pilatus 300 K).

The steady-state PL emission was measured with a fluorescence spectrometer (PerkinElmer LS 55). The perovskite films were deposited on FTO/cp-$TiO_2$/mp-$TiO_2$/$SnO_2$ as substrates, and all samples were pulsed by using a supercontinuum laser source with an excitation wavelength of 420 nm. TRPL spectroscopy was performed with a Fluorolog TCSPC at an excitation wavelength of 640 nm (HORIBA). The lifetime was obtained by fitting the TRPL results with a bi-exponential decay function:

$$R(t) = B_1 \exp\left(-\frac{t}{\tau_1}\right) + B_2 \exp\left(-\frac{t}{\tau_2}\right) \quad \text{(Equation 2)}$$

Absorbance was measured with an integrating sphere using UV-vis spectroscopy (PerkinElmer Lambda 950S). XPS measurements were performed using a conventional ultra-high vacuum XPS system, and the Mg Kα X-ray source (hν = 1253.6 eV) from a dual-anode X-ray gun was used. The spectra were recorded with a Phoibos 100 (SPECS) hemispherical electron analyzer. The XPS spectra were recorded at a pass-energy of 90 eV for the survey scan and 20 eV for the narrow scan in the fixed-analyzer transmission mode. The peak positions were corrected using C-1 s peak at 284.8 eV.

### Characterization

The solar cell measurements were performed with an Oriel solar simulator (450 W xenon, AAA class) and a Keithley 2400 source meter at room temperature. The light intensity was calibrated using a Si reference solar cell equipped with an IR-cutoff filter (KG3, Newport), and was recorded prior to the measurement. Current-voltage characteristics of the solar cells were obtained by applying an external voltage bias and measuring the current response with a digital source meter. The voltage scan rate was 100 mV $s^{-1}$, and no device preconditioning, such as light soaking or forward voltage bias applied for a long time, was applied before starting the measurement. The active areas of the solar cells were defined by a 0.16-$cm^2$, non-reflective, home-made, black-metal mask to reduce the influence of the scattered light. The EQE was measured with an IQE 200B (Oriel) without bias light. The SCLC measurements were obtained with a SP-200 (BioLogic) instrument in a dark environment with a bias from 0 to 2 V.

### X-ray crystallography

Colorless single crystals of [Bcim][TFSI] were obtained by slowly cooling the melting liquid of the IL from 120°C to room temperature. A suitable crystal of dimensions 0.29 × 0.25 × 0.10 $mm^3$ was selected and mounted on a SuperNova, Dual, Cu at home/near, Atlas diffractometer. The crystal was kept at T = 140.00(10) K during the data collection. The dataset was reduced and corrected for absorption with the help of a set of faces enclosing the crystal as snugly as possible and the latest available version of *CrysAlis*$^{Pro}$.[69] The structure was solved with the SHELXT[70] solution program using dual methods, with Olex2[71] as the graphical interface. The model was refined with SHELXL[72] using full-matrix least-squares minimization on $|F|^2$. The hydrogen atoms were found in a difference map and refined freely. Crystallographic and refinement data are summarized in Table S7. Crystallographic data have been deposited with the Cambridge Crystallographic Data Centre and correspond to code 2070505. These data can be obtained free of charge via https://www.ccdc.cam.ac.uk/data_request/cif, or by emailing data_request@ccdc.cam.ac.uk, or by contacting the Cambridge Crystallographic Data Centre, 12 Union Road, Cambridge CB2 1EZ, UK; fax: +44 1223 336033.

## SUPPLEMENTAL INFORMATION

Supplemental information can be found online at https://doi.org/10.1016/j.xcrp.2021.100475.

## ACKNOWLEDGMENTS

The authors thank the Swiss National Science Foundation, National Natural Science Foundation of China (no. 21761132007), and the China International Science and Technology Project (no. 2016YFE0114900) for financial support. X.-X.G. thanks the China Scholarship Council (CSC) fellowship (no. 201806250082) for financial support. H.K. thanks the SNSF (project no. 200020L_1729/1) for financial support. W.L. thanks the SNSF (Ambizione project PZ00P2_179989) for financial support. The 2D WAXS measurements were performed at SPring-8 with the approval of the JASRI (proposal no. 2019B1808). We thank Prof. Dunrun Zhu from Nanjing Tech University for valuable discussions about the X-ray structure of the IL.

## AUTHOR CONTRIBUTIONS

M.K.N., P.J.D., Y.F., Z.F., and X.-X.G. conceived the project. X.-X.G. and Z.F. designed the experiments, analyzed the data, and prepared the manuscript. X.-X.G. and B.D. carried out the film deposition and device fabrication. X.-X.G. carried out the characterizations, including SEM, XRD, and J-V. H.K. conducted the PL and TRPL tests. W.L. and A.Z. carried out the XPS measurements and analysis. Y.Z. assisted in the XRD test. N.S. performed the 2D WAXS measurements and analysis. F.F.T. and R.S. performed the X-ray structure analysis of the IL. All authors discussed the results and commented on the manuscript. M.K.N. and P.J.D. supervised the project.

## DECLARATION OF INTERESTS

The authors declare no competing interests.

Received: January 20, 2021
Revised: March 26, 2021
Accepted: June 2, 2021
Published: June 24, 2021

## REFERENCES


1. Kojima, A., Teshima, K., Shirai, Y., and Miyasaka, T. (2009). Organometal halide perovskites as visible-light sensitizers for photovoltaic cells. J. Am. Chem. Soc. *131*, 6050–6051.
2. National Renewable Energy Laboratory (2021). Best research-cell efficiency chart. https://www.nrel.gov/pv/cell-efficiency.html.
3. Jung, E.H., Jeon, N.J., Park, E.Y., Moon, C.S., Shin, T.J., Yang, T.-Y., Noh, J.H., and Seo, J. (2019). Efficient, stable and scalable perovskite solar cells using poly(3-hexylthiophene). Nature *567*, 511–515.
4. Min, H., Kim, M., Lee, S.-U., Kim, H., Kim, G., Choi, K., Lee, J.H., and Seok, S.I. (2019). Efficient, stable solar cells by using inherent bandgap of α-phase formamidinium lead iodide. Science *366*, 749–753.
5. Wang, R., Mujahid, M., Duan, Y., Wang, Z.-K., Xue, J., and Yang, Y. (2019). A review of perovskites solar cell stability. Adv. Funct. Mater. *29*, 1808843.
6. Urbina, A. (2020). The balance between efficiency, stability and environmental impacts in perovskite solar cells: A review. J. Phys. Energy. *2*, 022001.
7. Zhang, Y., Wang, P., Tang, M.-C., Barrit, D., Ke, W., Liu, J., Luo, T., Liu, Y., Niu, T., Smilgies, D.-M., et al. (2019). Dynamical transformation of two-dimensional perovskites with alternating cations in the interlayer space for high-performance photovoltaics. J. Am. Chem. Soc. *141*, 2684–2694.
8. Hamill, J.C., Schwartz, J., and Loo, Y.-L. (2018). Influence of solvent coordination on hybrid organic-inorganic perovskite formation. ACS Energy Lett. *3*, 92–97.
9. Ono, L.K., Liu, S.F., and Qi, Y. (2020). Reducing detrimental defects for high-performance metal halide perovskite solar cells. Angew. Chem. Int. Ed. Engl. *59*, 6676–6698.
10. Wang, H., Gong, X., Zhao, D., Zhao, Y.-B., Wang, S., Zhang, J., Kong, L., Wei, B., Quintero-Bermudez, R., Voznyy, O., et al. (2020). A multi-functional molecular modifier enabling efficient large-area perovskite light-emitting diodes. Joule *4*, 1977–1987.
11. Wu, W.-Q., Zhong, J.-X., Liao, J.-F., Zhang, C., Zhou, Y., Feng, W., Ding, L., Wang, L., and Kuang, D.-B. (2020). Spontaneous surface/interface ligand-anchored functionalization for extremely high fill factor over 86% in perovskite solar cells. Nano Energy *75*, 104929.
12. Yang, Z., Dou, J., Kou, S., Dang, J., Ji, Y., Yang, G., Wu, W.-Q., Kuang, D.-B., and Wang, M. (2020). Multifunctional phosphorus-containing lewis acid and base passivation enabling efficient and moisture-stable perovskite solar cells. Adv. Funct. Mater. *30*, 1910710.
13. Xia, J., Luo, J., Yang, H., Zhao, F., Wan, Z., Malik, H.A., Shi, Y., Han, K., Yao, X., and Jia, C. (2020). Vertical phase separated cesium fluoride doping organic electron transport layer: A facile and efficient "bridge" linked heterojunction for perovskite solar cells. Adv. Funct. Mater. *30*, 2001418.
14. Torimoto, T., Tsuda, T., Okazaki, K., and Kuwabata, S. (2010). New frontiers in materials science opened by ionic liquids. Adv. Mater. *22*, 1196–1221.
15. Jia, X., Zuo, C., Tao, S., Sun, K., Zhao, Y., Yang, S., Cheng, M., Wang, M., Yuan, Y., Yang, J., et al. (2019). $CsPb(I_xBr_{1-x})_3$ solar cells. Sci. Bull. (Beijing) *64*, 1532–1539.
16. Wang, A., Deng, X., Wang, J., Wang, S., Niu, X., Hao, F., and Ding, L. (2021). Ionic liquid reducing energy loss and stabilizing $CsPbI_2Br$ solar cells. Nano Energy *81*, 105631.
17. Seo, J.-Y., Matsui, T., Luo, J., Correa-Baena, J.-P., Giordano, F., Saliba, M., Schenk, K., Ummadisingu, A., Domanski, K., Hadadian, M., et al. (2016). Ionic liquid control crystal growth to enhance planar perovskite solar cells efficiency. Adv. Energy Mater. *6*, 1600767.
18. Huang, X., Guo, H., Wang, K., and Liu, X. (2017). Ionic liquid induced surface trap-state passivation for efficient perovskite hybrid solar cells. Org. Electron. *41*, 42–48.
19. Leblanc, A., Mercier, N., Allain, M., Dittmer, J., Pauporté, T., Fernandez, V., Boucher, F., Kepenekian, M., and Katan, C. (2019). Enhanced stability and band gap tuning of α-$[HC(NH_2)_2]PbI_3$ hybrid perovskite by large cation integration. ACS Appl. Mater. Interfaces *11*, 20743–20751.
20. Chen, C., Song, Z., Xiao, C., Awni, R.A., Yao, C., Shrestha, N., Li, C., Bista, S.S., Zhang, Y., Chen, L., et al. (2020). Arylammonium-assisted reduction of the open-circuit voltage deficit in wide-bandgap perovskite solar cells: The role of suppressed ion migration. ACS Energy Lett. *5*, 2560–2568.
21. Shu, H., Xia, J., Yang, H., Luo, J., Wan, Z., Malik, H.A., Han, F., Yao, X., and Jia, C. (2020). Self-assembled hydrophobic molecule-based surface modification: A strategy to improve efficiency and stability of perovskite solar cells. ACS Sustain. Chem.& Eng. *8*, 10859–10869.
22. Salado, M., Ramos, F.J., Manzanares, V.M., Gao, P., Nazeeruddin, M.K., Dyson, P.J., and Ahmad, S. (2016). Extending the lifetime of perovskite solar cells using a perfluorinated dopant. ChemSusChem *9*, 2708–2714.
23. Zhang, Y., Fei, Z., Gao, P., Lee, Y., Tirani, F.F., Scopelliti, R., Feng, Y., Dyson, P.J., and Nazeeruddin, M.K. (2017). A strategy to produce high efficiency, high stability perovskite solar cells using functionalized ionic liquid-dopants. Adv. Mater. *29*, 1702157.
24. Li, M., Zhao, C., Wang, Z.-K., Zhang, C.-C., Lee, H.K.H., Pockett, A., Barbé, J., Tsoi, W.C., Yang, Y.-G., Carnie, M.J., et al. (2018). Interface modification by ionic liquid: a promising candidate for indoor light harvesting and stability improvement of planar perovskite solar cells. Adv. Energy Mater. *8*, 1801509.
25. Xia, R., Fei, Z., Drigo, N., Bobbink, F.D., Huang, Z., Jasiūnas, R., Franckevičius, M., Gulbinas, V., Mensi, M., Fang, X., et al. (2019). Retarding thermal degradation in hybrid perovskites by ionic liquid additives. Adv. Funct. Mater. *29*, 1902021.
26. Bai, S., Da, P., Li, C., Wang, Z., Yuan, Z., Fu, F., Kawecki, M., Liu, X., Sakai, N., Wang, J.T.-W., et al. (2019). Planar perovskite solar cells with long-term stability using ionic liquid additives. Nature *571*, 245–250.
27. Xia, R., Gao, X.-X., Zhang, Y., Drigo, N., Queloz, V.I.E., Tirani, F.F., Scopelliti, R., Huang, Z., Fang, X., Kinge, S., et al. (2020). An efficient approach to fabricate air-stable perovskite solar cells via addition of a self-polymerizing ionic liquid. Adv. Mater. *32*, e2003801.
28. Wu, X., Zhang, L., Xu, Z., Olthof, S., Ren, X., Liu, Y., Yang, D., Gao, F., and Liu, S. (2020). Efficient perovskite solar cells via surface passivation by a multifunctional small organic ionic compound. J. Mater. Chem. A Mater. Energy Sustain. *8*, 8313–8322.
29. Wang, S., Li, Z., Zhang, Y., Liu, X., Han, J., Li, X., Liu, Z., Liu, S., and Choy, W.C.H. (2019). Water-soluble triazolium ionic-liquid-induced surface self-assembly to enhance the stability and efficiency of perovskite solar cells. Adv. Funct. Mater. *29*, 1900417.
30. Lin, Y.-H., Sakai, N., Da, P., Wu, J., Sansom, H.C., Ramadan, A.J., Mahesh, S., Liu, J., Oliver, R.D.J., Lim, J., et al. (2020). A piperidinium salt stabilizes efficient metal-halide perovskite solar cells. Science *369*, 96–102.
31. Deng, X., Xie, L., Wang, S., Li, C., Wang, A., Yuan, Y., Cao, Z., Li, T., Ding, L., and Hao, F. (2020). Ionic liquids engineering for high-efficiency and stable perovskite solar cells. Chem. Eng. J. *398*, 125594.
32. Zhang, H., Shi, Y., Yan, F., Wang, L., Wang, K., Xing, Y., Dong, Q., and Ma, T. (2014). A dual functional additive for the HTM layer in perovskite solar cells. Chem. Commun. (Camb.) *50*, 5020–5022.
33. Yang, D., Yang, R., Ren, X., Zhu, X., Yang, Z., Li, C., and Liu, S.F. (2016). Hysteresis-suppressed high-efficiency flexible perovskite solar cells using solid-state ionic-liquids for effective electron transport. Adv. Mater. *28*, 5206–5213.
34. Yang, D., Zhou, X., Yang, R., Yang, Z., Yu, W., Wang, X., Li, C., Liu, S., and Chang, R.P.H. (2016). Surface optimization to eliminate hysteresis for record efficiency planar perovskite solar cells. Energy Environ. Sci. *9*, 3071–3078.
35. Freire, M.G., Neves, C.M.S.S., Marrucho, I.M., Coutinho, J.A.P., and Fernandes, A.M. (2010). Hydrolysis of tetrafluoroborate and hexafluorophosphate counter ions in imidazolium-based ionic liquids. J. Phys. Chem. A *114*, 3744–3749.
36. Cao, Y., and Mu, T. (2014). Comprehensive investigation on the thermal stability of 66 ionic liquids by thermogravimetric analysis. Ind. Eng. Chem. Res. *53*, 8651–8664.
37. Xue, Z., Qin, L., Jiang, J., Mu, T., and Gao, G. (2018). Thermal, electrochemical and radiolytic stabilities of ionic liquids. Phys. Chem. Chem. Phys. *20*, 8382–8402.
38. Rodrigues, M.-T.F., Babu, G., Gullapalli, H., Kalaga, K., Sayed, F.N., Kato, K., Joyner, J., and Ajayan, P.M. (2017). A materials perspective on

Li-ion batteries at extreme temperatures. Nat. Energy *2*, 17108.

39. Kenneth, R.S., Annegret, S., and María-José, T. (2000). Influence of chloride, water, and organic solvents on the physical properties of ionic liquids. Pure Appl. Chem. *72*, 2275–2287.

40. Scammells, P.J., Scott, J.L., and Singer, R.D. (2005). Ionic liquids: the neglected issues. Aust. J. Chem. *58*, 155–169.

41. Dash, P., and Scott, R.W.J. (2009). 1-Methylimidazole stabilization of gold nanoparticles in imidazolium ionic liquids. Chem. Commun. (Camb.) (7), 812–814.

42. Lazarus, L.L., Riche, C.T., Malmstadt, N., and Brutchey, R.L. (2012). Effect of ionic liquid impurities on the synthesis of silver nanoparticles. Langmuir *28*, 15987–15993.

43. Yan, N., Fei, Z., Scopelliti, R., Laurenczy, G., Kou, Y., and Dyson, P.J. (2010). Crystallisation of inorganic salts containing 18-crown-6 from ionic liquids. Inorg. Chim. Acta *363*, 504–508.

44. Williams, D.B., Stoll, M.E., Scott, B.L., Costa, D.A., and Oldham, W.J., Jr. (2005). Coordination chemistry of the bis(trifluoromethylsulfonyl)imide anion: molecular interactions in room temperature ionic liquids. Chem. Commun. (Camb.) (11), 1438–1440.

45. Prodius, D., and Mudring, A.-V. (2018). Rare earth metal-containing ionic liquids. Coord. Chem. Rev. *363*, 1–16.

46. Vij, A., Wilson, W.W., Vij, V., Corley, R.C., Tham, F.S., Gerken, M., Haiges, R., Schneider, S., Schroer, T., and Wagner, R.I. (2004). Methyl tin(IV) derivatives of $HOTeF_5$ and $HN(SO_2CF_3)_2$: a solution multinuclear NMR study and the X-ray crystal structures of $(CH_3)_2SnCl(OTeF_5)$ and $[(CH_3)_3Sn(H_2O)_2][N(SO_2CF_3)_2]$. Inorg. Chem. *43*, 3189–3199.

47. Rocher, N.M., Izgorodina, E.I., Rüther, T., Forsyth, M., Macfarlane, D.R., Rodopoulos, T., Horne, M.D., and Bond, A.M. (2009). Aluminium speciation in 1-butyl-1-methylpyrrolidinium bis(trifluoromethylsulfonyl)amide/$AlCl_3$ mixtures. Chemistry *15*, 3435–3447.

48. Wehmschulte, R.J., Peverati, R., and Powell, D.R. (2019). Convenient access to gallium(I) cations through hydrogen elimination from cationic gallium(III) hydrides. Inorg. Chem. *58*, 12441–12445.

49. Fei, Z., Zhao, D., Pieraccini, D., Ang, W.H., Geldbach, T.J., Scopelliti, R., Chiappe, C., and Dyson, P.J. (2007). Development of nitrile-Functionalized ionic liquids for C-C coupling reactions: Implication of carbene and nanoparticle catalysts. Organometallics *26*, 1588–1598.

50. Liu, J., Shirai, Y., Yang, X., Yue, Y., Chen, W., Wu, Y., Islam, A., and Han, L. (2015). High-quality mixed-organic-cation perovskites from a phase-pure non-stoichiometric intermediate $(FAI)_{1-x}$-$PbI_2$ for solar cells. Adv. Mater. *27*, 4918–4923.

51. Zhu, T., Zheng, D., Rager, M.-N., and Pauporté, T. (2020). The stabilization of formamidinium lead tri-Iodide perovskite through a methylammonium-based additive for high-efficiency solar cells. Sol, RRL. *4*, 2000348.

52. Raga, S.R., Jung, M.-C., Lee, M.V., Leyden, M.R., Kato, Y., and Qi, Y. (2015). Influence of air annealing on high efficiency planar structure perovskite solar cells. Chem. Mater. *27*, 1597–1603.

53. Schulz, P., Edri, E., Kirmayer, S., Hodes, G., Cahen, D., and Kahn, A. (2014). Interface energetics in organo-metal halide perovskite-based photovoltaic cells. Energy Environ. Sci. *7*, 1377–1381.

54. Sadoughi, G., Starr, D.E., Handick, E., Stranks, S.D., Gorgoi, M., Wilks, R.G., Bär, M., and Snaith, H.J. (2015). Observation and mediation of the presence of metallic lead in organic-inorganic perovskite films. ACS Appl. Mater. Interfaces *7*, 13440–13444.

55. Birkhold, S.T., Precht, J.T., Liu, H., Giridharagopal, R., Eperon, G.E., Schmidt-Mende, L., Li, X., and Ginger, D.S. (2018). Interplay of mobile ions and injected carriers creates recombination centers in metal halide perovskites under bias. ACS Energy Lett. *3*, 1279–1286.

56. Motti, S.G., Meggiolaro, D., Barker, A.J., Mosconi, E., Perini, C.A.R., Ball, J.M., Gandini, M., Kim, M., De Angelis, F., and Petrozza, A. (2019). Controlling competing photochemical reactions stabilizes perovskite solar cells. Nat. Photonics *13*, 532–539.

57. Cho, K.T., Grancini, G., Lee, Y., Oveisi, E., Ryu, J., Almora, O., Tschumi, M., Schouwink, P.A., Seo, G., Heo, S., et al. (2018). Selective growth of layered perovskites for stable and efficient photovoltaics. Energy Environ. Sci. *11*, 952–959.

58. Chiang, C.-H., and Wu, C.-G. (2018). A method for the preparation of highly oriented $MAPbI_3$ crystallites for high-efficiency perovskite solar cells to achieve an 86% Fill Factor. ACS Nano *12*, 10355–10364.

59. Zhao, X., Tao, L., Li, H., Huang, W., Sun, P., Liu, J., Liu, S., Sun, Q., Cui, Z., Sun, L., et al. (2018). Efficient planar perovskite solar cells with improved fill factor via interface engineering with graphene. Nano Lett. *18*, 2442–2449.

60. Bube, R.H. (1962). Trap density determination by space-charge-limited currents. J. Appl. Physiol. *33*, 1733–1737.

61. Li, M., Li, B., Cao, G., and Tian, J. (2017). Monolithic $MAPbI_3$ films for high-efficiency solar cells via coordination and a heat assisted process. J. Mater. Chem. A Mater. Energy Sustain. *5*, 21313–21319.

62. Choudhury, A.R., Winterton, N., Steiner, A., Cooper, A.I., and Johnson, K.A. (2005). In situ crystallization of low-melting ionic liquids. J. Am. Chem. Soc. *127*, 16792–16793.

63. Holbrey, J.D., Reichert, W.M., and Rogers, R.D. (2004). Crystal structures of imidazolium bis(trifluoromethanesulfonyl)imide 'ionic liquid' salts: the first organic salt with a cis-TFSI anion conformation. Dalton Trans. (15), 2267–2271.

64. Gilli, G., and Gilli, P. (2000). Towards an unified hydrogen-bond theory. J. Mol. Struct. *552*, 1–15.

65. Kato, Y., Toledo, L.M., and Rebek, J. (1996). Energetics of a low barrier hydrogen bond in nonpolar solvents. J. Am. Chem. Soc. *118*, 8575–8579.

66. Butler, K.T., Svane, K., Kieslich, G., Cheetham, A.K., and Walsh, A. (2016). Microscopic origin of entropy-driven polymorphism in hybrid organic-inorganic perovskite materials. Phys. Rev. B *94*, 180103.

67. Svane, K.L., Forse, A.C., Grey, C.P., Kieslich, G., Cheetham, A.K., Walsh, A., and Butler, K.T. (2017). How strong is the hydrogen bond in hybrid perovskites? J. Phys. Chem. Lett. *8*, 6154–6159.

68. Feng, J., Zhu, X., Yang, Z., Zhang, X., Niu, J., Wang, Z., Zuo, S., Priya, S., Liu, S.F., and Yang, D. (2018). Record efficiency stable flexible perovskite solar cell using effective additive assistant strategy. Adv. Mater. *30*, e1801418.

69. Rigaku (2020). CrysAlisPro: User-inspired software for single-crystal X-ray diffractometers (Rigaku), 2020.

70. Sheldrick, G. (2015). SHELXT-Integrated space-group and crystal-structure determination. Acta Crystallogr. A *71*, 3–8.

71. Dolomanov, O.V., Bourhis, L.J., Gildea, R.J., Howard, J.A.K., and Puschmann, H. (2009). OLEX2: a complete structure solution, refinement and analysis program. J. Appl. Cryst. *42*, 339–341.

72. Sheldrick, G.M. (2015). Crystal structure refinement with SHELXL. Acta Crystallogr. C Struct. Chem. *71*, 3–8.